Phase transition induced recrystallization and low surface potential barrier leading to 10.91% efficient CsPbBr3 perovskite solar cells

1 **Phase transition induced recrystallization and low surface potential barrier**

2 **leading to 10.91%-efficient CsPbBr₃ perovskite solar cells**

3 Guoqing Tong[a,b], Taotao Chen[b], Huan Li[b], Longbin Qiu[a], Zonghao Liu[a], Yangyang

4 Dang[a], Wentao Song[a], Luis K. Ono[a], Yang Jiang[b,*], and Yabing Qi[a,*]

5 [a] *Energy Materials and Surface Sciences Unit (EMSSU), Okinawa Institute of Science*

6 *and Technology Graduate University (OIST), 1919-1 Tancha, Onna-son, Kunigami-*

7 *gun, Okinawa 904-0495, Japan*

8 *E-Mail: Yabing.Qi@OIST.jp

9

10 [b] *School of Materials Science and Engineering, Hefei University of Technology, Hefei*

11 *230009, P. R. China*

12 *E-Mail: apjiang@hfut.edu.cn

13

14 **ABSTRACT:**

15 High efficiency and long-term stability are vital for further development of perovskite

16 solar cells (PSCs). PSCs based on cesium lead halide perovskites exhibit better stability

17 but lower power conversion efficiency (PCE), compared with organic-inorganic hybrid

18 perovskites. Lower PCE is likely associated with trap defects, overgrowth of partial

19 crystals and irreversible phase transition in the films. Here we introduce a strategy to

20 fabricate high-efficiency CsPbBr₃-based PSCs by controlling the ratio of CsBr and

21 PbBr₂ to form the perovskite derivative phases (CsPb₂Br₅/Cs₄PbBr₆) via a vapor growth

22 method. Following post-annealing, the perovskite derivative phases as nucleation sites

23 transform to the pure CsPbBr₃ phase accompanied by crystal rearrangements and retard

24 rapid recrystallization of perovskite grains. This growth procedure induced by phase

25 transition not only makes the grain size of perovskite films more uniform, but also

26 lowers the surface potential barrier existing between the crystals and grain boundaries.

27 Owing to the improved film quality, a PCE of 10.91% was achieved for n-i-p structured

28 PSCs with silver electrodes, and a PCE of 9.86% for hole-transport-layer-free devices

29 with carbon electrodes. Moreover, the carbon electrode-based devices exhibited an

30 excellent long-term stability and retained 80% of initial efficiency in ambient air for

31 more than 2000 h without any encapsulation.

32 **Keywords**

33 Perovskite solar cell, derivative phases, CsPbBr$_3$, phase transition, recrystallization,

34 vapor deposition

35

1. Introduction

37 The incredible development of organic-inorganic hybrid perovskite solar cells (PSCs)

38 in the past decade has attracted tremendous attention from both academia and industry.

39 From the initial power conversion efficiency (PCE) of 3.8% to the very recently

40 certified record of 24.2%[1-5], processing technique including solution method[6-8],

41 vapor deposition[9-12], hybrid deposition[13-15], hybrid chemical vapor

42 deposition[16-22], methylamine gas based method[23-27], vapor & solution[28-30]

43 and anti-solvent crystallization[24, 31] *etc*. have been employed to produce the highly

44 crystalline and uniform perovskite films[32]. Unfortunately, volatility of the organic

45 materials (MA$^+$/FA$^+$) and weak bonding energy between metal cations and halide

46 anions render the organic-inorganic hybrid PSCs to decompose easily under condition

47 such as humidity, heat, electric filed and light illumination, which impedes the

48 commercial applications[7, 33, 34]. To alleviate the instability issue, the substitution

49 of organic cations with inorganic ones such as cesium (Cs) and rubidium (Rb) to

50 construct all inorganic perovskites has been demonstrated to effectively improve the

51 stability of PSCs [29, 35].

52 CsPbI$_3$ as the representative material of the inorganic perovskite CsPbX$_3$ (X=Cl, Br

53 and I) shows a suitable optical bandgap of 1.73 eV, and the champion PCE is up to

54 17.06%[36, 37]. However, the desired cubic perovskite phase (α-CsPbI$_3$) is only stable

55 at high temperatures (＞300 °C) and spontaneously transforms to the non-perovskite

56 yellow phase (δ-CsPbI$_3$) under ambient environment[38, 39]. Although several

57 strategies have been developed to improve the durability of CsPbI$_3$-based PSCs (e.g.,

58 HI induced growth, solvent-controlled, gradient Br doping *etc*.), the stability is still far

59 away to meet the requirement for practical applications [33, 39, 40]. Currently, an all

60 inorganic CsPbBr$_3$-PSC with a hole transport layer (HTL) free architecture is proposed

61 by employing carbon paste as counter electrode with an initial PCE of 6.7%, which can

survive in the humid environment for 2640 h[41].The replacement of iodine (I) with a smaller atomic radius such as bromine (Br) can decrease the structure deviation, resulting in an effective enhancement of perovskite durability[42]. However, the low PCE of $CsPbBr_3$-based PSCs is still an important issue due to the large optical absorption loss from the wide bandgap and severe recombination caused by inferior film quality.

To overcome these drawbacks, several strategies have been proposed to improve the overall PCE and simultaneously prolong the thermal stability of inorganic PSCs. For example, gradient architecture to accelerate hole extraction [40, 42-44], interface modification (i.e., derivative phases, quantum dots, ions doping B-site) to prolong carrier lifetimes [45, 46]. Regarding to the recombination, a high number of defects at the interface and grain boundaries usually act as charge recombination centers in the devices because the decomposition of crystals at the grain boundaries is more easily than that in the inner of the film seven under a lower temperature and/or humid condition, which significantly impedes charge carrier transport, resulting in a poor performance [47]. On the other hand, different with hybrid perovskites treated in a lower post-annealing temperature, a higher temperature treatment over 300 °C are necessary for the inorganic counterparts, which results in a fast and straight forward growth of crystals, leading to a poor crystallintiy with uneven crystal size, large traps and stress concentration in the films. Thus, it is important to fabricate high quality $CsPbBr_3$ films with a reduced defect density, uniform grain sizes to achieve highly efficient of $CsPbBr_3$-based PSCs.

In this work, we propose a phase transition induced (PTI) method to produce high quality $CsPbBr_3$ thin films by utilizing the derivative phases as nucleation sites to slow down the formation of $CsPbBr_3$ grains and release the stress concentration in order to achieve a high quality and compact perovskite film. In this method, core-shell structured films containing derivative phases, i.e., $CsPbBr_3@CsPb_2Br_5$ and $CsPbBr_3@Cs_4PbBr_6$ are first deposited on the substrates by the sequential vapor deposition method. After that, thermal annealing induced phase transition enables the formation of cubic $CsPbBr_3$ recrystallization films (denoted as PTI-$CsPbBr_3$) from

92   CsPb$_2$Br$_5$ and Cs$_4$PbBr$_6$ to novel CsPbBr$_3$ at the grain boundaries. Based on this

93   growth procedure, the PTI-CsPbBr$_3$ films showed larger grain size, improved

94   uniformity with high crystallization and a reduced trap density, as well as lower surface

95   potential barrier between the crystals and grain boundaries. As a result, a champion

96   PCE of 10.91% was achieved for n-i-p structured CsPbBr$_3$-based PSCs, and a PCE of

97   9.86% was also realized for HTL-free carbon electrode based PSCs. Furthermore, the

98   carbon electrode based PSC exhibits a markedly stability improvement in both

99   humidity and thermal attacks and retains 80% of initial performance after 2000 h.
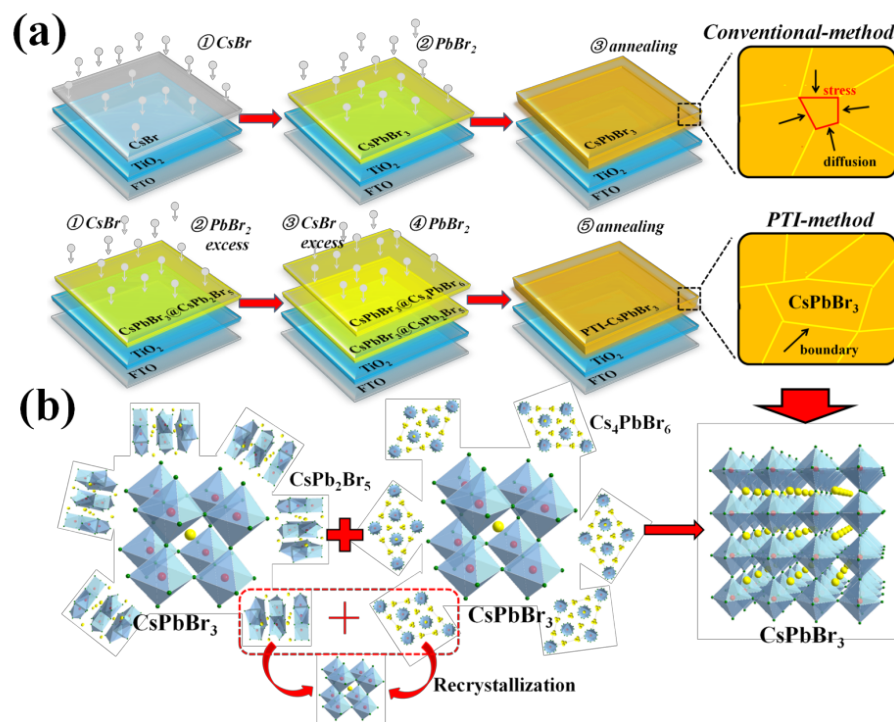
100

101   **Fig. 1. (**a) The conventional and phase transition induced (PTI) methods for the CsPbBr$_3$ thin film;

102   (b) The formation from the derivative phase (CsPb$_2$Br$_5$/Cs$_4$PbBr$_6$) to the CsPbBr$_3$ inorganic

103   perovskite phase.

104

2.   Results and discussion

2.1 Characterization of PTI-CsPbBr$_3$ thin films and phase transition

107   **Fig. 1**a illustrates the formation of the CsPbBr$_3$ films by the conventional and PTI

108   methods. Different from the conventional deposition procedure, we first prepare the

109   CsPbBr$_3$@CsPb$_2$Br$_5$ core-shell structured layer by sequentially depositing the CsBr and

110   excess $PbBr_2$ in the PTI-method. Atop the $CsPbBr_3$@$CsPb_2Br_5$ layer, we deposit excess

111   CsBr and $PbBr_2$ by sequential vapor deposition to form the $CsPbBr_3$@Cs_4PbBr_6 thin

112   film. As seen in **Fig. S1**, the co-existence phases can be found in the pristine films and

113   the corresponding atomic ratios of each element extracted from XPS measurements

114   listed in **Table S1**, which agrees with our previous results[42, 47, 48]. **Fig. 1**b shows

115   the corresponding phase transformation schematic drawing, in which $CsPbBr_3$ shows a

116   three-dimensional (3D) cubic phase. $CsPb_2Br_5$ presents a two-dimensional (2D)

117   tetragonal structure, and the Cs ions are sandwiched between two layers of Pb-Br

118   coordination polyhedrons [47]. In turn, Cs_4PbBr_6 has a zero-dimensional (0D) crystal

119   structure based on the $[PbBr_6]^{4-}$ octahedron, in which the octahedrons are separated

120   from each other by CsBr bridges [48]. The presence of the derivative phases (i.e.,

121      $CsPb_2Br_5$ and Cs_4PbBr_6) around the $CsPbBr_3$ crystals facilitate the inorganic perovskite

122   film formation during the post-annealing process, which is ascribed to inter-diffusion

123   of the excess $PbBr_2$ in the $CsPb_2Br_5$ and excess CsBr in Cs_4PbBr_6 phase.

124
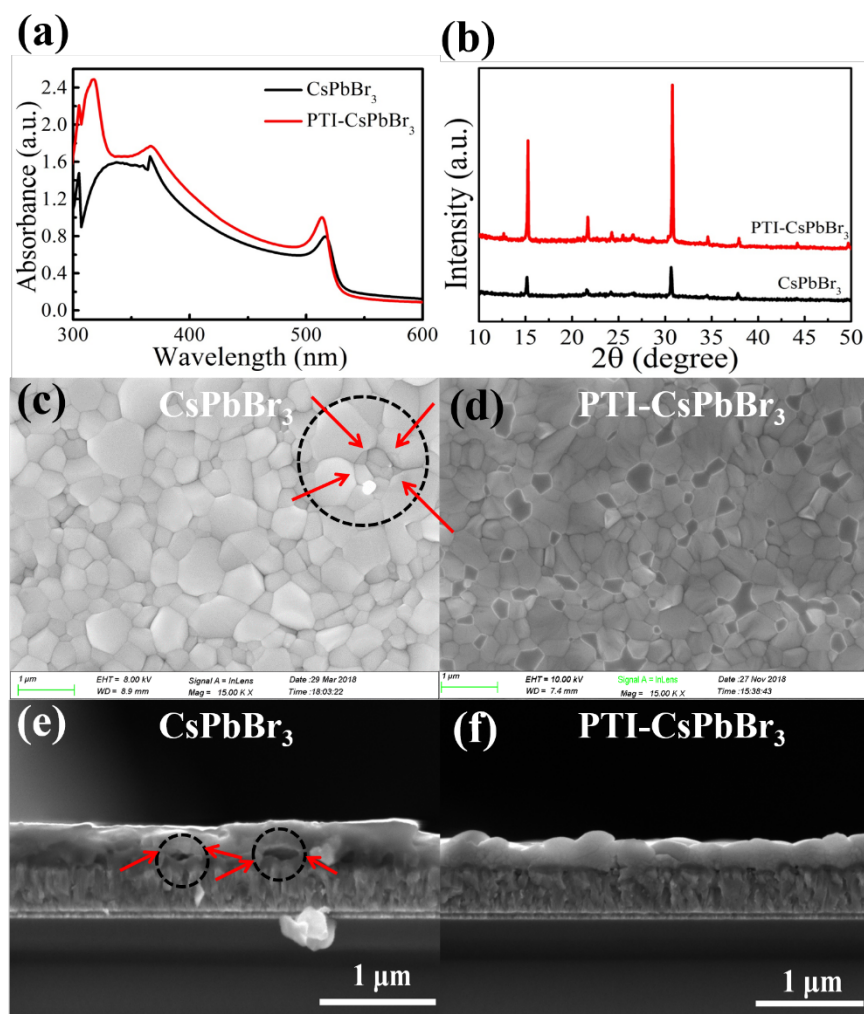
Fig. 2. (a) Absorption spectra and (b) XRD patterns of the CsPbBr$_3$ and PTI-CsPbBr$_3$ films; Scanning electron microscopy (SEM) images of (c) the CsPbBr$_3$ and (d) PTI-CsPbBr$_3$ films; Cross-section SEM images of (e) the CsPbBr$_3$ and (f) PTI-CsPbBr$_3$ films.

To get detailed understanding of the above proposed phase transformation process, we carefully check the photophysics, morphological and crystallographic properties of CsPbBr$_3$ and PTI-CsPbBr$_3$ films. **Fig. S4-S5** show the optical images of the CsPbBr$_3$ and PTI-CsPbBr$_3$ films annealed under different temperatures. It is observed that both cases turn into dark yellow with increasing the annealing temperature, and becomes light yellow at a higher temperature. As seen in **Fig. S6**, when the temperature is above 350 $^\circ$C, the absorption of the films decreased significantly due to the large pinholes (**Fig. S7-S8**). **Fig. 2**a shows the absorption spectra of the CsPbBr$_3$ and PTI-CsPbBr$_3$ films, in which the stronger light absorption at the short wavelength can be explained

by the high crystallinity and uniform grain size. The absorption edge of both films is located at ~ 550 nm, which is consistent with previous reports via the solution method [41, 49]. The corresponding optical bandgap values of the conventional $CsPbBr_3$ and PTI-$CsPbBr_3$ films are determined to be 2.35 and 2.37 eV, respectively, from a plot of $(\alpha h\nu)^2$ versus the photon energy ($h\nu$) using the Kubelka-Munk equations (**Fig. S9**) [50]. The negligible bandgap change indicates that the derivative phase converts to the $CsPbBr_3$ phase after annealing. Accompanied by the grain growth during the annealing procedure, we also find that the morphologies of the pre-preparation films are quite different at various annealing temperatures. In **Fig. S7-S10**, the uniform and compact films with gradually enlarged grain sizes are observed by the increase of annealing temperature (above 300 $^{\circ}$C), compared to the pristine films at room temperature (RT). However, many pinholes can be found in the films after the treatment at an even higher temperature due to the decomposition of the inorganic perovskite, which significantly affects the light harvesting and forms the leakage path. Different from the conventional $CsPbBr_3$ film at the RT with a grain size of ~ 200 nm, the PTI-$CsPbBr_3$ film shows a smaller grain size, which is attributed to the top layer of $CsPbBr_3@Cs_4PbBr_6$ with lower crystallinity. Interestingly, as the annealing temperature increases, the grains of PTI-$CsPbBr_3$ grow quickly with high crystallinity in the film and much smaller crystallites can be detected clearly at the grain boundaries, which are formed by the phase transition. On the basis of the EDS spectra (in **Fig. S11**), it can be inferred that the ratio of Cs, Pb and Br is closed to 1:1:3, which suggests that the materials at grain boundaries correspond to the newly formed $CsPbBr_3$ crystallites as the result of phase transition. In parallel, it is worth noting that the grain size of the PTI-$CsPbBr_3$ film is significantly more uniform after annealing, as can be seen in **Fig. 2**d. On the contrary, overgrowth of partial crystals in the conventional $CsPbBr_3$ film (**Fig. 2**c) is observed due to fast reaction and uneven growth. The grain sizes are increased by the grain boundary diffusion during annealing. As large grains come into contact with each other and grow further, the grains extrude each other as illustrated in **Fig. 2**c (the red line indicates the direction of grain boundary diffusion), which impedes the grain boundaries diffusion and results in the stress concentration at the grain boundaries. In

169   the SEM cross-section images (**Fig. 2**e-f), we can see that the conventional $CsPbBr_3$

170   film has a full coverage but poor crystallinity. The extrusion of the grains against each

171   other results in partial convex grains, leaving a large number of pinholes between the

172   substrate and $CsPbBr_3$ film. In contrast, the PTI-controlled film exhibits a high

173   crystallinity, uniform and full coverage film after post-annealing. To further understand

174   the component and phase transition of inorganic perovskite, we analyze the X-ray

175   diffraction (XRD) patterns of pre-films at different annealing temperatures

176   with/without the PTI treatment. As presented in **Fig. 2**b and **Fig. S12-S15**, for the

177   conventional $CsPbBr_3$ film, the typical peaks at 15.20^o, 21.55^o, 30.66^o, 34.37^o and

178   37.77^o are detected and can be assigned to (100), (110), (200), (210) and (211). In turn,

179   the $CsPbBr_3$ film grown by the PTI method is substantially different. At the room

180   temperature (RT) condition, partial CsBr and $PbBr_2$ can't react completely, resulting in

181   a derivative phase in the film. The peaks at $11.65°$, $24.05°$and $29.38°$ can be assigned

182   to the $CsPb_2Br_5$ phase and other diffraction peaks located at $22.41°$ and $28.60°$ are

183   assigned to Cs_4PbBr_6 (**Fig. S12**). As the annealing temperature increases, the peaks

184   become shaper, which indicates that the high annealing temperature can accelerate the

185   inter-diffusion and reaction of CsBr and $PbBr_2$ to form the pure $CsPbBr_3$ and also

186   promote the crystal growth into larger grains. On the other hand, many crystallites exist

187   in the perovskite grains because of the polycrystalline nature of the perovskite films. It

188   is worth noting that the full-width at half-maximum (FWHM) of (100) and (200)

189   reflections decreases after the PTI treatment. The corresponding crystallite sizes are

190   determined by using Scherrer equation (see in **Table S2**), and the crystallinites size

191   increase from 68.01 nm and 57.73 nm to 94.25 nm and 69.65 nm, respectively, which

192   indicates that large crystallite sizes are obtained in the $PTI-CsPbBr_3$ grains. We also

193   find that the PL spectra of the $PTI-CsPbBr_3$ films are enhanced gradually as the

194   annealing temperature increases and drops remarkably after being treated at even

195   higher temperatures (**Fig. S16**). It is reported that $CsPb_2Br_5$ and Cs_4PbBr_6 are the

196   indirect bandgap materials with PL forbidden by their symmetry [51-53]. The

197   corresponding lifetime of $PTI-CsPbBr_3$ films are increased from 1.03 ns to 4.45 ns after

198   annealing at 350 ^{o}C for 30 min (in **Fig. S16**). This improvement indicates that the high

quality perovskite films provide high crystallinity and fewer traps at the grain boundaries after post-annealing.

How to understand the rearrangement of crystals induced by the phase transition? Firstly, Cs_4PbBr_6 can be viewed as the CsBr-rich component material and transformed into the cubic $CsPbBr_3$ phase with a side-product of CsBr at the grain boundary in the humid and heat treatment as follows:[53] $Cs_4PbBr_6 \rightarrow CsPbBr_3 + 3CsBr$. Additionally, CsBr has a higher melting point above 600 °C, thus it can't be evaporated during the annealing process. In contrast, the annealing temperature (from RT to 450 °C) accelerates the diffusion of CsBr into the inner film. Similarly, $CsPb_2Br_5$ is regarded as the CsBr-deficient material (or the $PbBr_2$-rich material) and can be converted into the $CsPbBr_3$ phase with the presence of $PbBr_2$ at the grain boundary under post-treatment with a heating temperature above 300 °C[54]. The equation can be described as follows:[47] $CsPb_2Br_5 \rightarrow CsPbBr_3 + PbBr_2$. It is worth noting that $PbBr_2$ has a melting temperature close to 357 °C, which ensures the chemical component and promotes its reaction with excess CsBr to construct the new $CsPbBr_3$ phase, if the treatment at a moderate temperature of ~350 °C[55]. Upon further annealing treatment ($>$400 °C), the sublimation of $PbBr_2$ and also the decomposition of $CsPbBr_3$ occur, which significantly influence the coverage of the obtained thin film, such as leaving pinholes in the film. This process can be described by the following equation: $CsPbBr_3 \rightarrow CsBr + PbBr_2$. A moderate annealing temperature ensures the complete reaction between $CsPb_2Br_5$ and Cs_4PbBr_6 to form the novel $CsPbBr_3$ at the ground boundaries as well as benefits the crystal growth into lager grains. As seen in **Fig. 3**b, during the annealing process, the derivative phase can serve as extra heterogeneous nucleation sites, which effectively slow down the formation of $CsPbBr_3$ crystals. Because the highly crystalline $CsPbBr_3$ is formed by reaction process between $CsPb_2Br_5$ and Cs_4PbBr_6, instead of fast growth of $CsPbBr_3$ directly. This effectively retards the perovskite growth rate, which markedly enhances the $CsPbBr_3$ film quality with lower traps than in the case of the inadequate reaction/fast reaction. On the other hand, this phase transition from 2D-$CsPb_2Br_5$ and 0D-Cs_4PbBr_6 to 3D structure of

CsPbBr$_3$ provides enough space for the perovskite grains to release the stress concentration, which is beneficial for reducing the surface potential.
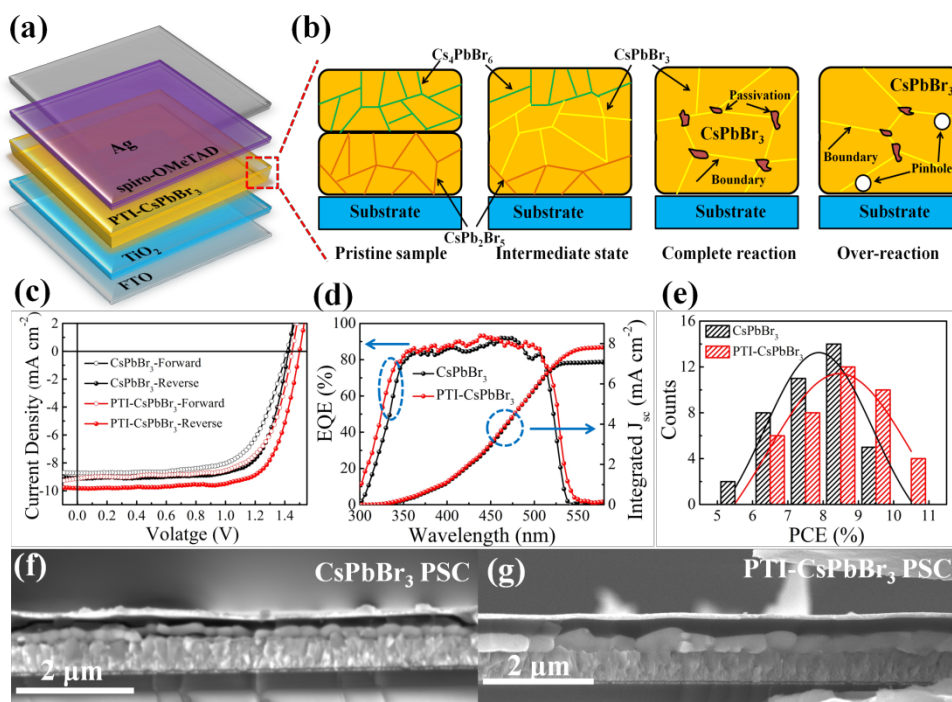
Fig. 3. (a) Device structure of a PTI-CsPbBr$_3$PSC; (b) Phase transition mechanism; (c) J-V curves of the CsPbBr$_3$ PSC and PTI-CsPbBr$_3$ PSC under forward and reverse scanning; (d) The corresponding EQE spectra and integrated J$_{sc}$; (e) Histograms of the PCEs of 40 devices for the CsPbBr$_3$ PSC and PTI-CsPbBr$_3$ PSC; Cross section SEM images of (f) the CsPbBr$_3$ PSC and (g) PTI-CsPbBr$_3$ PSC.

Table 1

Performance of the champion devices (CsPbBr$_3$ and PTI-CsPbBr$_3$) under forward and reverse scanning.

| Scanning	V_{oc} (V)	J_{sc} (mA cm^{-2})	FF (%)	PCE (%)
CsPbBr$_3$-Forward	1.414	8.58	68.91	8.36
CsPbBr$_3$-Reverse	1.423	9.35	71.63	9.53
PTI-CsPbBr$_3$-Forward	1.452	9.08	69.70	9.19
PTI-CsPbBr$_3$-Reverse	1.498	9.78	74.47	10.91

2.2 Photovoltaic performance of PTI-CsPbBr$_3$ PSCs

242 Conventional inorganic PSCs are constructed with a planar architecture of FTO/c-

243 TiO$_2$/inorganic perovskite/spiro-OMeTAD/Ag (**Fig. 3**a). **Fig. 3**f-g show the cross-

244 sectional-view SEM image of the inorganic PSCs. It is observed that the conventional

245 CsPbBr$_3$ or PTI-CsPbBr$_3$ film with an approximate thickness of 300 nm is homogenous

246 and dense and sandwiched between the electron transport layer of TiO$_2$ and hole

247 transport layer of spiro-OMeTAD. The photovoltaic performances of inorganic

248 CsPbBr$_3$ PSCs formulated by the PTI and conventional method are given in **Fig. S17-**

249 **S18** and **Tables S3-S4**. It is found that the performance of devices increases

250 significantly with suitable annealing temperature and drops after high thermal attacks.

251 Thus, we can obtain an optimal annealing temperature of 350 $^{\circ}$C to ensure a high

252 photovoltaic performance for PSCs. As depicted in **Fig. 3**b, the lower annealing

253 temperature is unable to promote the inter-diffusion of CsPb$_2$Br$_5$ and Cs$_4$PbBr$_6$ to

254 achieve phase transition to CsPbBr$_3$ for PTI-CsPbBr$_3$ case, which results in poor light

255 harvesting and carrier transport, leading to a low efficiency. Similarly, a high density

256 of pinholes in the films after the treatment at a higher temperature results in a poor

257 morphology, which can be explained by the decomposition of perovskite films.

258 Furthermore, pinholes create shunting paths leading to a poor performance. The current

259 density-voltage (J-V) curves for champion devices of PTI-CsPbBr$_3$and conventional

260 CsPbBr$_3$ are shown in **Fig. 3**c. The open-circuit voltage (V$_{oc}$), photocurrent density (J$_{sc}$)

261 and fill factor (FF) of PTI-CsPbBr$_3$ PSC increase considerably by 75 mV, 0.53 mA cm$^-$

262 ^{2} and 2.84%, respectively. The corresponding PCE of the best performing device

263 increases from 9.53% (V$_{oc}$=1.423 V, J$_{sc}$=9.35 mA cm^{-2} and FF=71.63%) to a

264 breakthrough performance 10.91% (V$_{oc}$=1.498 V, J$_{sc}$=9.78 mA cm^{-2} and FF=74.47%)

265 under reverse scanning. To our best knowledge, this value is the highest performance

266 for the CsPbBr$_3$-based PSCs. The corresponding external quantum efficiencies (EQE)

267 are carried out and presented in **Fig. 3**d. The photoresponse edges of the devices are

268 close to 550 nm, which agrees with the absorption spectra and shows a slight red-shift.

269 As previously reported[56, 57], the reflection of light by the electrode and/or the FTO

270 substrate, or some other interfaces in the perovskite devices are not considered when

271 performing UV-vis measurements of bare perovskite films may lead to the slight red-

shift of the EQE spectrum as compared with the absorption spectrum, which were observed in both our work and several previous works[49, 58, 59]. The EQE values for both cases, in the visible region from 300 nm to 500 nm, exceed 80% with an integrated photocurrent density of 7.09 mA cm^{-2} (conventional CsPbBr$_3$), and 7.81 mA cm^{-2} (PTI-CsPbBr$_3$), respectively. It is close to the photocurrent density extracted from J-V curves. Additionally, the steady PCE of devices approaching 9.01% and 10.35% for CsPbBr$_3$ and PTI-CsPbBr$_3$ PSCs, respectively, are recorded under a bias voltage at the maximum power point for 200 s (**Fig. S19**), which agrees well with the value from J-V curves. It should be noted that only minor hysteresis effects are observed in the J-V measurements for the devices (**Fig. 3**c). In addition, this PTI-procedure exhibits good reproducibility, as seen in **Fig. 3**e, the efficiency of PTI-CsPbBr$_3$ PSCs ranging from 6.5% to 10.9% for 40 devices and presents a relatively higher PCE than that of conventional CsPbBr$_3$ PSCs.

Additionally, we construct a solar cell device based on the HTL-free architecture employing the carbon as counter electrode (**Fig. 4**a), where the absence of organic HTL and the usage of carbon electrodes can improve the stability of PSCs [60-62]. The cross-sectional-view SEM image of the HTL-free device (**Fig. 4**b) shows that the continuous and uniform perovskite film with full coverage can effectively block the recombination between the absorption layer and carbon electrode, reducing the leakage path in PSCs. The observed good contact between the carbon paste and perovskite layer enables a high current extraction. As a result, an impressive PCE of 9.86% under forward scanning is obtained (**Fig. 4**c). The corresponding steady-state PCE is up to 9.15% as shown in **Fig. S20**. **Fig. 4**d and **Table S5** provide a comprehensive comparison of the PCE and device storage lifetime between this work and previously reported studies on CsPbBr$_3$-based PSCs [41, 45, 49,58, 63-71].
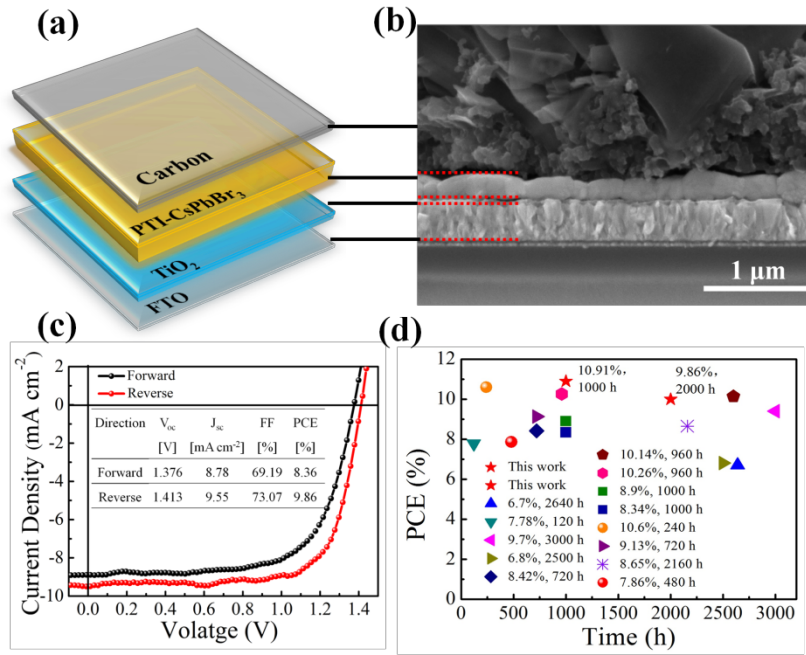
Fig. 4. Schematic drawing showing (a) the hole transport layer (HTL) free device structure of thePTI-CsPbBr$_3$ and (b) the corresponding cross section SEM; (c) J-V curves of the PTI-CsPbBr$_3$ PSCs with HTL-free under forward and reverse scanning; (d) Comparison of the PCE and device storage lifetime between this work and previously reported studies on CsPbBr$_3$-based PSCs. More details can be found in Supplementary Table S5.
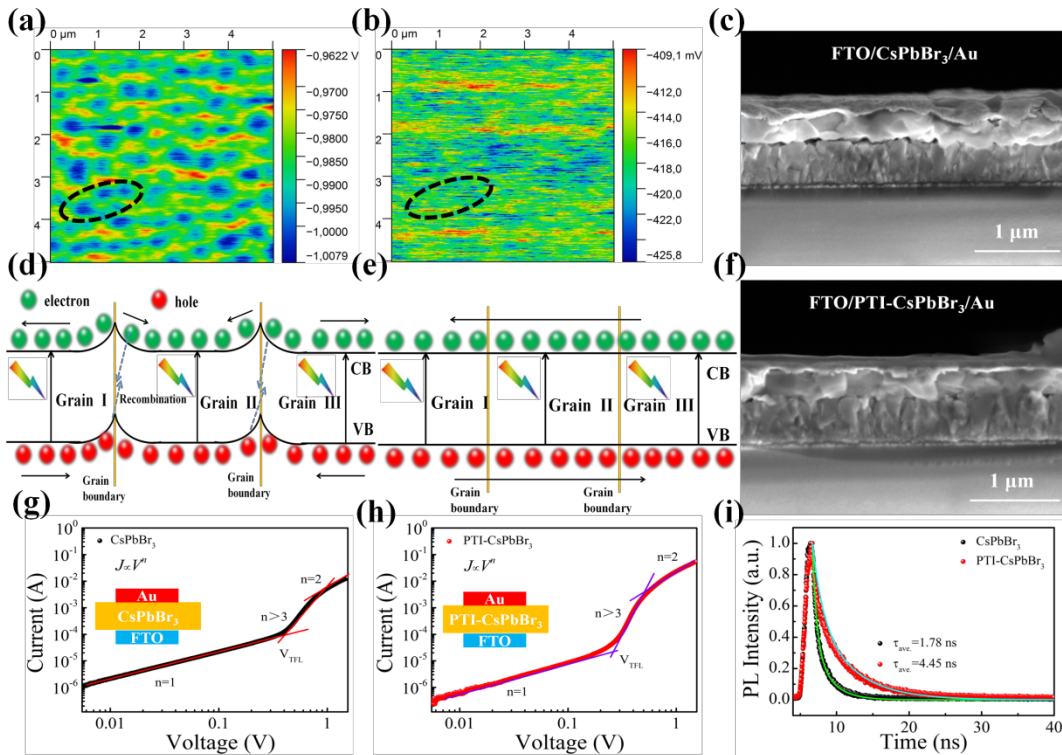
Fig. 5. Kelvin probe force microscopy (KPFM) images of (a) the CsPbBr$_3$ and (b) PTI-CsPbBr$_3$

films; (c) Cross section SEM images of the devices with $FTO/CsPbBr_3/Au$; Carrier transport mechanism of (d) the $CsPbBr_3$ and (e) $PTI-CsPbBr_3$ films; (f) Cross section SEM images of the devices with $FTO/PTI-CsPbBr_3/Au$; Current density-voltage (J-V) characteristics of devices with (g) the $FTO/CsPbBr_3/Au$ and (h) $FTO/PTI-CsPbBr_3/Au$ architecture; (i) Time resolved photoluminescence (TRPL) decay curves of the $CsPbBr_3$ and $PTI-CsPbBr_3$ films under 375 nm photon excitation.

2.3 Surface potential and carrier transport of PTI-CsPbBr₃ thin films

In general, the low PCE or poor stability of inorganic perovskite based PSCs are due to a large number of defects and unstable phases in the perovskite film during the formation. This is because the required high temperature annealing for the perovskite formation usually induce uneven growth of perovskite grains, which increases the stress concentration at the grain boundaries and also accelerates the overgrowth of partial perovskite crystals. Therefore, it may result in a large number of traps and metastable phase [30, 72, 73]. Thus we perform the surface investigation later to further understand the surface potential and carrier transport properties caused the rearrangement of crystals during the phase transition.

It is worth noting that the phase transition during the annealing processing providing a self-passivation at the grain boundaries, which shows a significant influence on the performance of devices. To further identify the self-passivation and understand the carrier transport behavior, we conduct a surface potential measurement by Kelvin probe force microscopy (KPFM). As shown in **Fig. S21**, the grain size of the PTI-$CsPbBr_3$ film is uniform, which provides an ultra-smooth surface with a root-mean-square roughness (RMS) of 13.75 nm. On the contrary, the grain size in the conventional $CsPbBr_3$ film is substantially larger and some grains are overgrown, which results in a substantially larger roughness of 20.55 nm. The surface potential mappings of the $CsPbBr_3$ films prepared by PTI and conventional method are presented in **Fig. 5**a-b and **Fig. S22**. The distribution of blue spots in the conventional $CsPbBr_3$ film is discontinuity and surrounded by the yellow patterns suggesting that the surface potential at the grain boundaries is higher than that in the crystals due to the overgrowth

of partial crystals (as depicted in **Fig. 1**a and **Fig. 2**c)[74]. However, the film produced by the PTI method giving a uniform distribution without any remarkable spots indicates that the lower surface potential barrier exists between the crystals and the grain boundaries. **Fig. S23** presents the contact potential difference (CPD) statistical distribution for conventional and PTI-CsPbBr$_3$ films. The absolute valueof average potentials for conventional CsPbBr$_3$ and PTI-CsPbBr$_3$ are 0.993 V and 0.418 V, respectively, which indicates that the PTI-CsPbBr$_3$ film shows a lower surface potential than the conventional CsPbBr$_3$ film. The potential barrier between the grain boundary and crystal implies a remarkable effect on the carrier transport. **Fig. 5**d-e show the schematic band diagrams for the conventional CsPbBr$_3$ and PTI-CsPbBr$_3$ film under illumination. The presence of three blue spots from the overgrown grains indicates that the three grains are connected with each other and the holes are accumulated at the grain boundary due to the existence of the potential barrier in the film. This accumulation will lower the valance and conduction band of the perovskite film at the grain boundaries, which impedes the electron transport and results in a large number of the recombination at the grain boundary [74,75]. In contrast, the appearance of the recrystallization phase at the grain boundary gives a uniform surface potential in the PTI-CsPbBr$_3$ film, which ensures the energy band consistency. It will benefit the electrons and holes transport to the counter electrode without any recombination at the grain boundaries. To verify this hypothesis , a time resolved photoluminescence (TRPL) is carried out and recorded in **Fig. 5**i. The curves are fitted by the equation: [65, 76]

$$\tau_{ave} = \frac{B_1 \tau_1^2 + B_2 \tau_2^2}{B_1 \tau_1 + B_2 \tau_2}$$

where B$_1$ and B$_2$ are the amplitudes, τ_1 and τ_2 represent the nonradioactive recombination and radiative recombination, respectively. The average lifetime of conventional CsPbBr$_3$ film is shorter than the PTI case, which confirms that the trap defects in the film are effectively suppressed by the recrystallization phases. To further evaluate the carrier transport behavior and defect density within the films, we construct a simple architecture by inserting the CsPbBr$_3$ thin film (with a thickness of 300 nm) between FTO and gold (FTO/inorganic perovskite/Au) as seen in **Fig. 5**c and f. The

evolutions of the space-charge limited current (SCLC) are tested under different bias voltage (**Fig. 5**g-h). The corresponding trap-filled limit voltages (V_{TFL}) can be extracted from the following equation:[24]

$$V_{TFL} = \frac{N_\tau eL^2}{2\varepsilon\varepsilon_0}$$

where N_τ is the trap density. ε is defined as dielectric constants of $CsPbBr_3$ perovskite (ε=16.46) and ε_0 is the vacuum permittivity with the value of $8.8\times10^{-12}\,F \cdot m^{-1}$. The e and L are the electron charge, and the corresponding thickness of the perovskite film. Here the V_{TFL} of the conventional $CsPbBr_3$ and PTI-$CsPbBr_3$ devices are 0.40 V and 0.25 V, respectively. The corresponding defect densities are estimated to be 8.06×10^{15} cm^{-3} and 5.04×10^{15} cm^{-3} for the $CsPbBr_3$ film with/without PTI treatment, showing a significantly reducing defects traps due to the high crystallinity of perovskite films and boundary passivation after recrystallization.
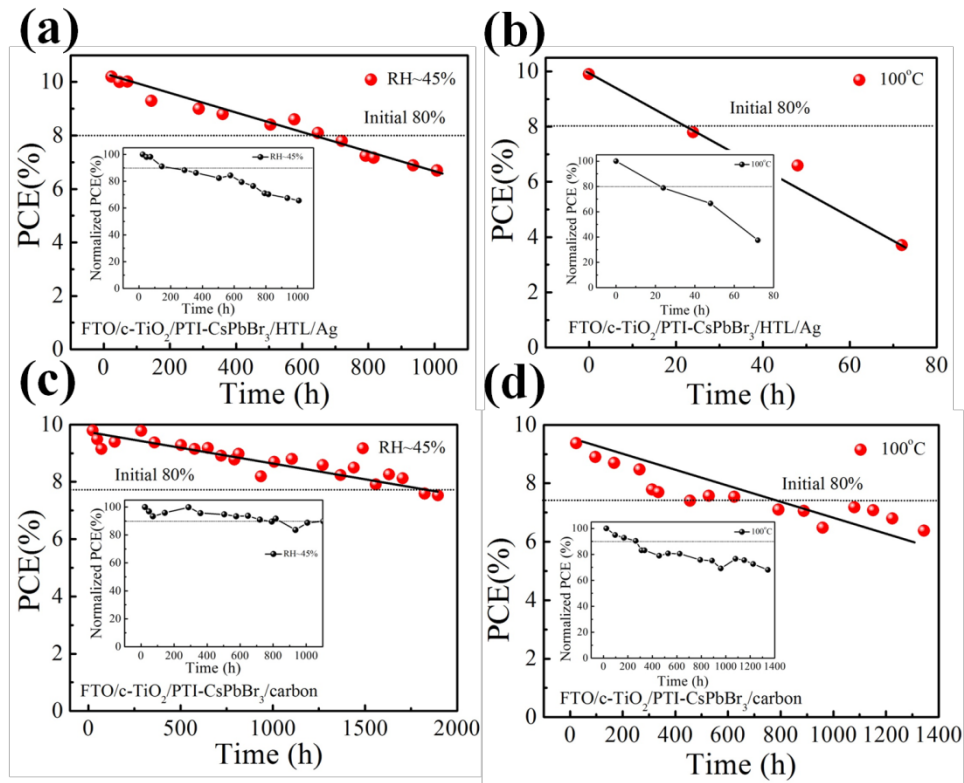
Fig. 6. Stability of PTI-$CsPbBr_3$ PSCs with HTL layer under (a) the humid environment (RH~45%) and (b) the heat condition (100ºC); Stability of the PTI-$CsPbBr_3$ PSCs without HTL layer under (c) the humid environment (RH~45%) and (d) the heat condition (100ºC).

2.4 Stability and degradation of PTI-CsPbBr₃ PSCs

382   Inorganic PSCs showing a good long-term stability, especially the CsPbBr$_3$-based

383   devices, has been verified by previous reports and demonstrated with slight

384   degradation under the high humid/heat condition [41, 49]. To check the stability of our

385   devices, we track the stability in both persistent humid and heat condition without any

386   encapsulation. As depicted in **Fig. 6**, the performance of the device with HTL layer

387   drops significantly under the thermal attacks due to the invalidation of spiro-OMeTAD,

388   instead of perovskite absorption layer. This is because the glass-transition temperature

389   (T$_g$) of spiro-OMeTAD is only 122 °C [77]. After introducing the additive such as Li

390   salt, the ideal working temperature of HTL layer would be less than 80 °C [78].

391   Compared with the high heating temperature, the low T$_g$ would make much trap sites

392   to be formed in the HTL layer [79]. Additionally, the metal electrode migration across

393   the spiro-OMeTAD layer into perovskite layer will induce the degradation of

394   perovskite film and form the leakage path [78]. These results can be verified by the

395   XRD results in **Fig. S24a**, in which the sample still preserves the perovskite structure

396   after being stored at 100 °C without any decomposition. In turn, the device with HTL

397   stored in the open air can still keep 80% of initial PCE for more than 1000 h. Notably,

398   the carbon-electrode-based device without HTL presents slight degradation in the

399   humid environment (90% of initial PCE after 1000 h and 80% of initial PCE after 2000

400   h), which demonstrates that the high stability against the moisture. At the same time

401   the device with carbon electrode also gives a superior performance at high temperature

402   and keeps over 60% of initial PCE after stored in the thermal equipment at 100 °C for

403   1400 h. The corresponding XRD patterns in **Fig. S24b** and **Fig. S25b** show that the

404   CsPbBr$_3$ films still keep high crystallinity after moisture and thermal attacks. The

405   decrease of device performance may be ascribed to the damage the carbon electrode

406   such as binder and conductive agent instead of the CsPbBr$_3$ films. Overall, these results

407   demonstrate that CsPbBr$_3$ is the potential candidate in boosting the photovoltaic

408   performance and stability of inorganic perovskite photovoltaic devices.

409

410   **3.   Conclusion**

In summary, we report a phase transition induced strategy to prepare CsPbBr$_3$ inorganic perovskite films. By introducing the derivative phase of CsPb$_2$Br$_5$ and Cs$_4$PbBr$_6$ as nucleation sites, a highly crystalline CsPbBr$_3$ film is obtained via crystal rearrangement after annealing. The PTI-CsPbBr$_3$ film also provides uniform grain sizes and self-passivation at the grain boundaries, which lowers the potential barrier between the crystal and grain boundary and reduces the trap defects, facilitating carrier transport. Finally, we successfully achieve the highest PCE of 10.91% for the CsPbBr$_3$ based PSCs, which also show high stability (over 2000 h in humidity and 1400 h in heat condition) in moisture and thermal attacks environment.

Appendix A. Supplementary material

Supplementary data associated with this article can be found in theonline version at http://dx.doi.org/10.1016/XXX.

References

[1] A. Kojima, K. Teshima, Y. Shirai, T. Miyasaka, J. Am. Chem. Soc.131 (2009), 6050-6051.

[2]https://www.nrel.gov/pv/assets/pdfs/best-research-cell-efficiencies-190416.pdf(2019).

[3] Q. Jiang, Y. Zhao, X. Zhang, X. Yang, Y. Chen, Z. Chu, Q. Ye, X. Li, Z. Yin,

441 J. You, Nat. Photonics.2019, DOI:10.1038/s41566-019-0398-2.

442 [4]S. Wu, R. Chen, S. Zhang, B. H. Babu, Y. Yue, H. Zhu, Z. Yang, C. Chen, W.

443 Chen, Y. Huang, S. Fang, T. Liu, L. Han, W. Chen, Nat. Commun. 10(2019) 1161-

444 1170.

445 [5] J. Xue, D. Yang, B. Cai, X. Xu, J. Wang, H. Ma, X. Yu, G. Yuan, Y. Zou, J.

446 Song, H. Zeng, Adv. Funct. Mater.29 (2019) 1807922-1807929.

447 [6] D. Bi, W. Tress, M. I. Dar, P. Gao, J. Luo, C. Renevier, K. Schenk, A. Abate,

448 F. Giordano, J. C. Baena, J. D. Decoppet, S. M. Zakeeruddin, M. K. Nazeeruddin, M.

449 Grätzel, A. Hagfeldt, Sci. Adv. 2(2016) e1501170.

450 [7] Y. Zhao, H. Tan, H. Yuan, Z. Yang, J. Z. Fan, J. Kim, O. Voznyy, X. Gong, L.

451 N. Quan, C. S. Tan, J. Hofkens, D. Yu, Q. Zhao, E. H. Sargent, Nat. Commun. 9(2018)

452 1607-1616.

453 [8] A. Swarnkar, A. R. Marshall, E. M. Sanehira, B. D. Chernomordik, D. T.

454 Moore, J. A. Christians, T. Chakrabarti, J. M. Luther, Science 354(2016) 92-95.

455 [9] M. Liu, M. B.Johnston, H. J. Snaith, Nature 501(2013) 395-398.

456 [10] G. Tong, H. Li, G. Li, T. Zhang, C. Li, L. Yu, J. Xu, Y. Jiang, Y. Shi, K. Chen,

457 Nano Energy 48(2018) 536-542.

458 [11] M. R. Leyden, L. K. Ono, S. R. Raga, Y. Kato, S. Wang, Y. B. Qi, J. Mater.

459 Chem. A 2(2014) 18742-18745.

460 [12] J. Ávila, C. Momblona, P. P. Boix, M. Sessolo, H. J. Bolink, Joule 1(2017)

461 431-442.

462 [13] L. K.Ono,S. Wang, Y.Kato, S. R.Raga,Y. B. Qi, Energy Environ. Sci. 7(2014)

463 3989-3993.

464 [14] S. Wang, L. K. Ono, M. R. Leyden, Y. Kato, S. R. Raga, M. V. Lee, Y. B.Qi,

465 J. Mater. Chem. A 3(2015) 14631-14641.

466 [15] S. Wang, X. Li, J. Wu, W. Wen, Y. B. Qi, Curr. Opin. Electrochem. 11(2015)

467 130-140.

468 [16] M. Leyden, L. K. Ono, S. Raga, Y. Kato, S. Wang, Y. B. Qi, J. Mater. Chem.

469 A 2(2014) 18742-18745.

470 [17] M. R. Leyden, M. V. Lee, S. R. Raga, Y. B. Qi, J. Mater. Chem. A 2(2015)

471 16097-16103.

472 [18] M. R. Leyden, Y.Jiang, Y. B. Qi, J. Mater. Chem. A 4(2016) 13125-13132.

473 [19] L. K. Ono, M. R. Leyden, S. Wang, Y. B. Qi, J. Mater. Chem. A 4(2016) 6693-

474 6713.

475 [20] M. R. Leyden, L. Meng, Y. Jiang, L. K. Ono, L. Qiu, E. J. Juárez-Pérez, C. Qin,

476 C.Adachi, Y. B. Qi, J. Phys. Chem. Lett. 8(2017) 3193-3198.

477 [21] A. Ng, Z. Ren, Q. Shen, S. H. Cheung, H. C. Gokkaya, S. K. So, A. B. Djurisic,

478 Y. Wan, X. Wu, C. Surya, ACS Appl. Mater. Interfaces 8(2016)32805-32814.

479 [22] G. Tong, Z. Song, C. Li, Y. Zhao, L. Yu, J. Xu, Y. Jiang, Y. Sheng, Y.

480 Shi,K.Chen, RSC Adv.7(2017) 19457-19463.

481 [23] S. R. Raga, L. K.Ono, Y. B. Qi, J. Mater. Chem. A, 4(2016) 2494-2500.

482 [24] Z. Liu, L. Qiu, E. J. Juarez-Perez, Z. Hawash, T. Kim, Y. Jiang, Z. Wu, S. R.

483 Raga, L. K.Ono, S. F. Liu, Y. B. Qi, Nat. Commun. 9(2018) 3880-3890.

484 [25] G. Tong, X. Lan, Z. Song, G. Li, H. Li, L. Yu, J. Xu, Y. Jiang, Y. Sheng, Y.

485 Shi, K. Chen, Mater. Today Energy, 5 (2017) 173-180.

486 [26] S. Pang, Y. Zhou, Z. Wang, M. Yang, A. R. Krause, Z. Zhou,K. Zhu, N. P.

487 Padture, G. Cui, J. Am. Chem. Soc. 138(2016) 750-753.

488 [27] S. R. Raga, Y. Jiang, L. K. Ono, Y. B. Qi, Energy Technology 5(2017) 1750-

489 1761.

490 [28] Q. Chen, H. Zhou, Z. Hong, S. Luo, H-S. Duan, H-H. Wang, Y. Liu, G. Li, Y.

491 Yang, J. Am. Chem. Soc. 136(2014) 622-625.

492 [29] Y. Jiang, M. R. Leyden, L. Qiu, S. Wang, L. K. Ono, Z. Wu, E. J. Juarez-Perez,

493 Y. B. Qi, Adv. Funct. Mater. 28(2018) 1703835-1703847.

494 [30] G. Tong, X. Geng, Y. Yu, L. Yu, J. Xu, Y. Jiang, Y. Sheng, Y. Shi, K. Chen,

495 RSC Adv. 7(2017) 18224-18230.

496 [31] M. Xiao, F. Huang, W. Huang, Y. Dkhissi, Y. Zhu, J. Etheridge, A. Gray-

497 Weale, U. Bach, Y-B. Cheng, L. Spiccia, Angew. Chem. Int. Ed. 53(2014)9898-9903.

498 [32] K. L. Gardner, J. G. Tait, T. Merckx, W. Qiu, U. W. Paetzold, L. Kootstra, M.

499 Jaysankar, R. Gehlhaar, D. Cheyns, P. Heremans, J. Poortmans, Adv. Energy Mater.

500 6(2016) 1600386.

501   [33] P. Wang, X. Zhang, Y. Zhou, Q. Jiang, Q. Ye, Z. Chu, X. Li, X. Yang,Z.Yin,

502 J. You, Nat. Commun. 9(2018) 2225-2231.

503   [34] W. Tress, M. Yavari, K. Domanski, P. Yadav, B. Niesen, J. P. Correa Baena, A.

504 Hagfeldt, M. Grätzel, Energy Environ. Sci. 11(2018) 151-165.

505   [35] J-W. Lee, D-H. Kim, H-S. Kim, S-W. Seo, S. M. Cho, N-G. Park, Adv. Energy

506 Mater. 5(2015) 1501310-1501318.

507   [36] Y. Wang, T. Zhang, M. Kan, Y. Zhao, J. Am. Chem. Soc. 140(2018) 12345-

508 12348.

509   [37] E. M. Sanehira, A. R. Marshall, J. A. Christians, S. P. Harvey, P. N. Ciesielski,

510 L. M. Wheeler, P. Schulz, L. Y. Lin, M. C. Beard, J. M. Luther, Sci. Adv.

511 3(2017)e4204.

512   [38]B. Li, Y. Zhang, L. Fu, T. Yu, S. Zhou, L. Zhang, L. Yin,Nat. Commun. 9(2018)

513 1076-1083.

514   [39] T. Zhang, M. I. Dar, G. Li, F. Xu, N. Guo, M. Grätzel, Y. Zhao, Sci. Adv.

515 3(2017) e1700841.

516   [40] H. Bian, D. Bai, Z. Jin, K. Wang, L. Liang, H. Wang, J. Zhang, Q. Wang,

517 S.Liu,Joule 2(2018) 1500-1510.

518   [41] J. Liang, C. Wang, Y. Wang, Z. Xu, Z. Lu, Y. Ma, H. Zhu, Y. Hu, C. Xiao, X.

519 Yi, G. Zhu, H. Lv, L. Ma, T. Chen, Z. Tie, Z. Jin,J. Liu, J. Am. Chem. Soc. 138(2016)

520 15829-15832.

521   [42] G. Tong, T. Chen, H. Li, W. Song, Y. Chang, J. Liu, L. Yu, J. Xu, Y. B. Qi, Y.

522 Jiang, Sol. RRL 3(2019) 1900030-1900098.

523   [43] Q. Ma, S. Huang, X. Wen, M. A. Green, A. W. Y. Ho-Baillie, Adv.

524 Mater.6(2016) 1502202-1502206.

525   [44] C. Liu, W. Li, C. Zhang, Y. Ma, J. Fan, Y. Mai, J. Am. Chem. Soc. 140(2018)

526 3825-3828.

527   [45] W. S. Subhani, K. Wang, M. Du, X. Wang, S. F. Liu, Adv. Energy Mater.

528 9(2019)1803785-1803793.

529   [46] F. Wang, X. Jiang, H. Chen, Y. Shang, H. Liu, J. Wei, W. Zhou, H. He, W.

530 Liu, Z. Ning, Joule 2(2018) 2732-2743.

[47] G. Tong, H. Li, D. Li, Z. Zhu, E. Xu, G. Li, L. Yu, J. Xu, Y. Jiang, Small 14(2018) 1702523-1702530.

[48] G. Tong, H. Li, Z. Zhu, Y. Zhang, L. Yu, J. Xu, Y. Jiang, J. Phys. Chem. Lett. 9(2018) 1592-1599.

[49] J. Duan, Y. Zhao, B. He, Q. Tang, Angew.Chem. Int. Ed. 57(2018) 3787-3791.

[50] M. Chen, M-G. Ju, A. D. Carl, Y. Zong, R. L. Grimm, J. Gu, X. C. Zeng, Y. Zhou, N. P. Padture,Joule 2(2018) 558-570.

[51] G. Li, H. Wang, Z. Zhu, Y. Chang, T. Zhang, Z. Song, Y. Jiang, Chem. Commun. 52(2016) 11296-11299.

[52] L. Wu, H. Hu, Y. Xu, S. Jiang, M. Chen, Q. Zhong, D. Yang, Q. Liu, Y. Zhao, B. Sun,Q. Zhao, Y. Yin, Nano Lett. 17(2017) 5799-5804.

[53] X. Chen, F. Zhang, Y. Ge, L. Shi, S. Huang, J. Tang, Z. Lv, L. Zhang, B. Zou, H. Zhong, Adv. Funct. Mater. 28(2018) 1706567.

[54] F. Palazon, S. Dogan, S. Marras, F. Locardi, I. Nelli, P. Rastogi, M. Ferretti, M. Prato, R. Krahne, L. Manna,J. Phys. Chem. C 121(2017) 11956-11961.

[55] I. Y. Zaitseva, I. S.Kovaleva, V. A. Fedorov,Russ. J. Inorg. Chem.51(2006) 619.

[56] Z. Chen, Q. Dong, Y. Liu, C. Bao, Y. Fang, Y. Lin, S. Tang, Q. Wang, X. Xiao, Y. Bai, Y. Deng, J. Huang, Nat. Commun. 8(2017) 1890.

[57] Z.Xiao, Q. Dong , C. Bi , Y. Shao , Y. Yuan, J. Huang, Adv. Mater. 26(2014) 6503.

[58] W. Chen, J. Zhang, G. Xu, R. Xue, Y. Li, Y. Zhou, J. Hou, Y. Li, Adv. Mater. 30(2018) 1800855-1800864.

[59] L. Zhou, X. Guo, Z. Lin, J. Ma, J. Su, Z. Hu, C. Zhang, S. F. Liu, J. Chang, Y. Hao, Nano Energy 60 (2019) 583-590.

[60] A. Mei, X. Li, L. Liu, Z. Ku, T. Liu, Y. Rong, M. Xu,M.Hu, J. Chen, Y. Yang, M. Grätzel, H. Han, Science 345(2014) 295-298.

[61] Z. Liu, M. Zhang, X. Xu, L. Bu, W. Zhang, W. Li, Z. Zhao, M. Wang, Y. Cheng, H. He, Dalton Trans. 44(2015)3967-3973.

[62] Z. Liu, A. Zhu, F. Cai, L. Tao, Y. Zhou, Z. Zhao, Q. Chen, Y. Cheng, H. Zhou, J. Mater. Chem. A 5(2017) 6597-6605.

[63] Y. Zhao, J. Duan, H. Yuan, Y. Wang, X. Yang, B. He, Q. Tang, Sol. RRL,3(2019)1800284-1800290.

[64] H. Li, G. Tong, T. Chen, H. Zhu, G. Li, Y. Chang, L. Wang, Y. Jiang, J. Mater. Chem. A 6(2018) 14255-14261.

[65] J. Duan, Y. Zhao, X. Yang, Y. Wang, B. He, Q. Tang, Adv. Energy Mater. 8(2018) 1802346-1802354.

[66] H. Yuan, Y. Zhao, J. Duan, Y. Wang, X. Yang, Q. Tang, J. Mater. Chem. A 6(2018) 24324-24329.

[67] J. Ding, J. Duan, C. Guo, Q. Tang, J. Mater. Chem. A 6(2018) 21999-22004.

[68] X. Liu, X. Tan, Z. Liu, H. Ye, B. Sun, T. Shi, Z. Tang, G. Liao, Nano Energy 56(2019) 184-195.

[69] H. Xu, J.Duan, Y. Zhao, Z. Jiao, B. He, Q. Tang, Journal of Power Sources 399(2018) 76-82.

[70] Q. Li, J. Bai, T. Zhang, C. Nie, J. Duan, Q. Tang, Chem. Commun. 54(2018) 9575-9578.

[71] J. Ding, Y. Zhao, J. Duan, B. He, Q. Tang, ChemSusChem 11(2018) 1432-1438.

[72] Y. Zong, Z. Zhou, M. Chen, N. P. Padture, Y. Zhou, Adv. Energy Mater. 27(2018) 1800997-1801005.

[73] T. Zhang, N. Guo, G. Li, X. Qian, Y. Zhao, Nano Energy 26(2016) 50-56.

[74] A. Dymshits, A. Henning, G. Segev, Y. Rosenwaks, L. Etgar,Sci. Rep. 5(2015) 8704-8709.

[75] L. K.Ono, Y. B. Qi, J. Phys. Chem. Lett. 7(2016) 4764-4794.

[76] H. Dong, Z. Wu, J. Xi, X. Xu, L. Zuo, T. Lei, X. Zhao, L. Zhang, X. Hou, A. K-Y. Jen, Adv. Funct. Mater. 28(2018) 1704836-1704844.

[77] B. Xu, J. Zhang, Y. Hua, P. Liu, L. Wang, C. Ruan, Y. Li, G. Boschloo, E. M. J. Johansson, L. Kloo, A. Hagfeldt, A. K-Y. Jen, L. Sun, Chem 2(2017)676-687.

[78] K. Domanski, J-P. Correa-Baena, N. Mine, M. K. Nazeeruddin, A. Abate, M. Saliba, W. Tress, A. Hagfeldt, M. Grätzel, ACS Nano 10(2016) 6306-6314.

590   [79] G-W. Kim, G. Kang, M. M. Byranvand, G-Y. Lee, T. Park, ACS Appl. Mater.

591   Interfaces 9(2017) 27720-27726.

592